Available online at www.sciencedirect.com
ScienceDirect
International Journal of Heat and Fluid Flow 28 (2007) 1327–1339
International Journal of HEAT AND FLUID FLOW
www.elsevier.com/locate/ijhff

Experimental study of turbulent round jet flow impinging on a square cylinder laid on a flat plate

Nam-Shin Kim *, André Giovannini

Institut de Mécanique des Fluides de Toulouse, Allée du Pr. Camille Soula, 31400 Toulouse, France

Received 15 December 2006; received in revised form 8 July 2007; accepted 9 July 2007
Available online 22 October 2007

Abstract

A turbulent axisymmetric air jet impinging on a square cylinder mounted on a flat plate has been studied experimentally. Turbulence statistics and flow's topology were investigated. When the surface was heated through uniform heat flux, local heat transfer coefficient was measured. The jet from a long round pipe, 75 pipe diameters (D) in length, at Reynolds number of 23,000, impinged vertically on the square cylinder ($3D \times 3D \times 43D$). Measurements were performed using particle image velocimetry, flow visualization using fluorescent dye and infrared thermography. The flow's topology demonstrated a three-dimensional recirculation after separating from the square cylinder and a presence of foci between the bottom corner and the recirculation's detachment line. The distribution of heat transfer coefficient was explained by the influence of these flow's structures and the advection of kinetic energy. On the impingement wall of the square cylinder, a secondary peak in heat transfer coefficient was observed. Its origin can be attributed to very pronounced shear production coupled with the external turbulence coming from the free jet.

Keywords: Turbulent impinging jet; Square cylinder; PIV; Infrared thermography; Visualization

1. Introduction

Impinging jets are widely used in industrial application because of their effective way of enhancing convection heat transfer. A number of studies have investigated the effect of impingement surface shape on flow and heat transfer characteristic with various geometries. The most frequently considered in previous studies were flat, convex or concave surface (Martin, 1977; Hrycak, 1981; Baughn and Shimizu, 1989; Gau and Chung, 1991; Viskanta, 1993; Cooper et al., 1993; Cornaro et al., 1999). These studies reported that heat transfer at the stagnation point was increased with increasing relative curvature and was relatively higher than for an equivalent jet impinging on a flat plate. As a more complex shape case, Mesbah (1996) and Parneix et al. (1999) studied on a cylindrical pedestal of which the diameter and the height were almost equal to the pipe diameter ($D/1.06$), which was aimed to simulate an electronic component. They found that the local Nusselt number distribution was radically different from the flat plate configuration since the stagnation Nusselt number was a local minimum. There exists also a considerable amount of published data for heat transfer and flow field of arrays of rectangular blocks (Martinuzzi and Tropea, 1993; Molki et al., 1995) and a square cylinder (Igarashi, 1985, 1986, 1987) in a channel flow.

On the other hand, study on impingement of jet on a square cylinder is less approached in spite of its similar configuration with real industrial devices, for example components within airplane engine or electronic devices that needed to be cooled down. In the present study, a round jet impinging vertically on a square cylinder mounted horizontally on a flat plate was experimentally investigated. Since the width and the length of the impingement surface of the square cylinder is larger than the diameter of the pipe ($3D \times 43D$), it is expected that the flow on the top surface

* Corresponding author. Tel.: +33 561285932; fax: +33 561285992.
E-mail addresses: kim@imft.fr (N.-S. Kim), giova@imft.fr (A. Giovannini).

0142-727X/$ - see front matter © 2007 Elsevier Inc. All rights reserved.
doi:10.1016/j.ijheatfluidflow.2007.07.004

Nomenclature

Bi	Biot number
c_p	specific heat at constant pressure
D	diameter of pipe
E	voltage
e	thickness
F	view factor
k	thermal conductivity, turbulent kinetic energy $\left(=\frac{1}{2}(u'^2+v'^2)\right)$
I	current
Nu	Nusselt number $(=h_{cv}D/k)$
r	radial direction
r_c	recovery coefficient
Re_j	Reynolds number $(=V_jD/v)$
u', v'	RMS. velocity fluctuation
$\overline{U}_m$	mean velocity $(=(\overline{U}^2+\overline{V}^2)^{0.5})$
V_j, V_{c0}	averaged mean velocity and center velocity at pipe exit
P_R, P_D	locations of reattachment and detachment
P_k	production of turbulent kinetic energy
X_r	reattachment length: distance between $x/D=1.5$ and P_R,

Subscripts

amb	ambient
aw	adiabatic wall
c	stainless steel foil
cam	infrared camera
cd	conduction
cn	natural convection
cv	forced convection
d	dynamic
is	polyurethan insulation block
j	jet
m	measured
p	wall
pl	acrylic plate
ray	radiation
ref	reference
s	static

Greek symbols

v	kinematic viscosity of fluid
σ	Stefan–Boltzmann constant

and beyond the square cylinder resemble impinging jet flow on a flat plate and turbulent backward-facing step (BFS) flow, respectively. However, compared to the traditional BFS flow, the separated flow from the square cylinder has larger RMS fluctuating velocity normal to the wall due to the characteristic of impinging jet. Moreover, the flow's expansion becomes a three-dimensional turbulent flow beyond the square cylinder. So, more complex flow structures and their different interactions with the wall are expected. These characteristics will contribute differently to the heat transfer rate.

The objective of the present study is to characterize global and local flow field around the square cylinder, using particle image velocimetry (PIV) and flow visualization, and is to accurately measure wall temperature field, using infrared thermography system. Then, we will analyze flow structure's topology and turbulence's role in the mechanisms of convection heat transfer near the stagnation point as well as in the recirculation region. Eventually, this study is aimed to create a database for finding optimal position of jet maximizing heat transfer rate and to validate CFD simulation with different turbulence models and heat transfer simulation code. This data base was requested for industrial application, cooling a part of airplane using jet.

2. Experimental apparatus and measurement techniques

A schematic diagram of the experimental setup is shown in Fig. 1. An air jet came out of a pipe 16 mm in inner diameter (D), 1 mm in thickness, 1.2 m in length giving a length/diameter ratio of $75D$. The air was supplied from the building air compressor. The flow rate was controlled by adjusting pressure regulators. For PIV measurement, the secondary flow rate of the seeding device is added to the main flow rate. These flow control devices were calibrated before hand. The uncertainty in flow rate measurement was less than $\pm 1.3\%$. A thermostat bath of HAAKE G was connected at the exit of the regulating valves to adjust the temperature of the jet (T_j) to ambient temperature (T_{amb}) within ± 0.1 K. The air was redistributed to a plenum chamber of 100 l consisting of a perforate plate, a screen and a honeycomb. The pipe was connected to the plenum chamber via a convergent nozzle with a contraction ratio of 10. The impingement target consists of a square cylinder of 48 mm ($3D$) in height, 48 mm ($3D$) in width and 690 mm ($43D$) in length and an acrylic flat plate, measuring $650 \times 650 \times 10\ \text{mm}^3$. The square cylinder was mounted on the plate. They were placed perpendicularly and symmetrically below the pipe with an accuracy of less than 0.1°. The jet-to-cylinder spacing (H) was $3D$. The dimension of the plate and the length of the square cylinder are believed to ensure a negligible edge effect. Reynolds number Re_j, based on the mean jet velocity ($V_j \simeq 21$ m/s) and the inner pipe diameter, was fixed at 23,000. At the pipe exit, velocity and turbulence intensity profiles measured using hot wire anemometer conformed to those for fully developed turbulent flow. The turbulence intensity level at the centerline (v'/V_j) was 4.0%.

The experimental setup for the heat transfer study was the same, except for the impingement target. A stainless steel foil (AISI304 Fe/Cr18/Ni10), having a thickness (e_c) of 45 μm, bonded to a polyurethane block with epoxy,

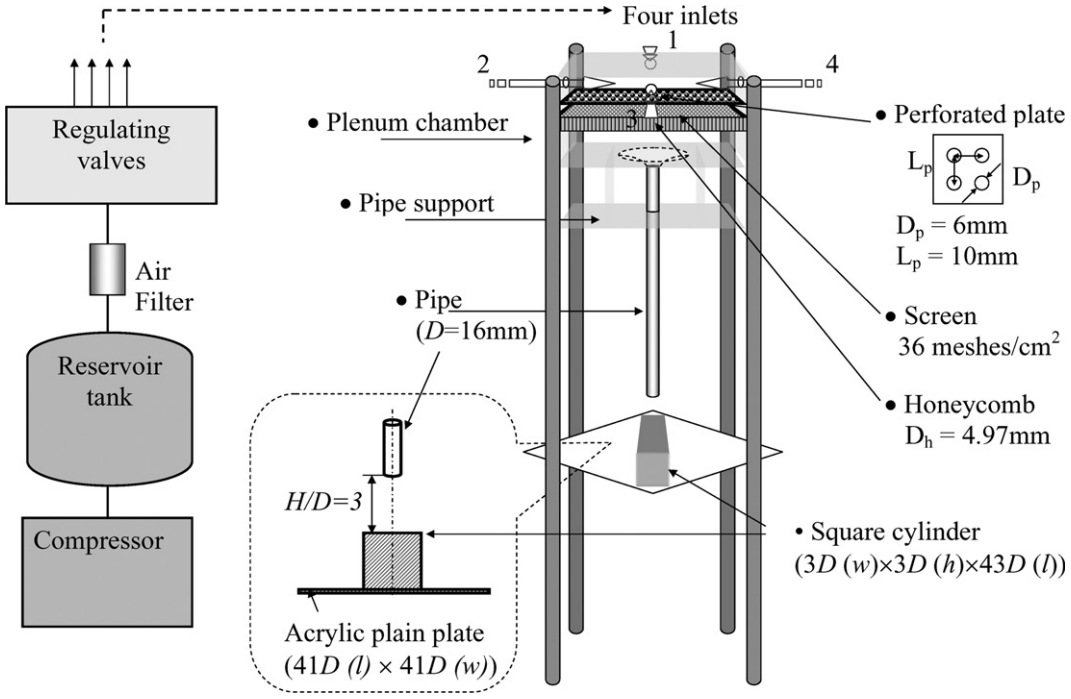

Fig. 1. Schematic of the experimental apparatus.

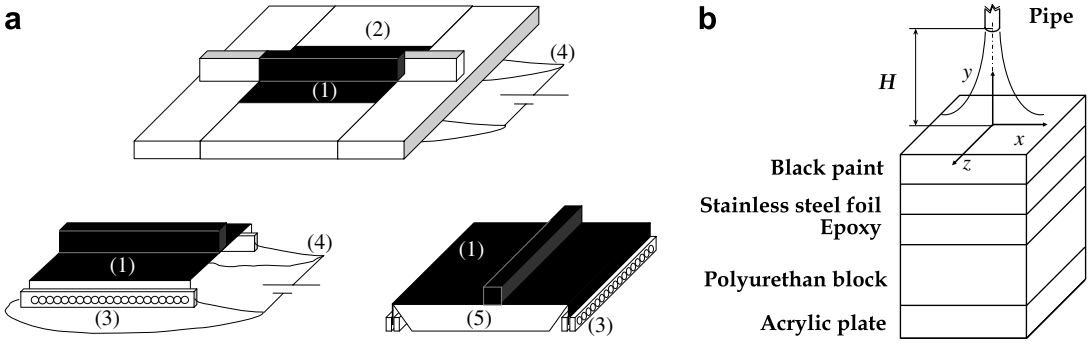

Fig. 2. Schematic of round jet impingement on a square cylinder (a) jet and test plate (b) heated test plate and coordinate system. (1) stainless steel foil, (2) styrofoam plate, (3) copper bar, (4) power supply, (5) polyurethan block.

was laid on the acrylic plate and heated by Joule effect (Fig. 2). The backward face was thus thermally isolated. The dimensions and thermal properties of the materials used are given in Table 1 (The thermal properties of the black paint and the epoxy are estimations from the work of Praisner et al., 2001). A set of copper bars was attached at both ends of the foil as an electric rod and was connected to a power supply. The good contact between the foil and the copper bar ensured a uniform heat flux in the stainless steel foil. The two ends of the foil were folded downward to prevent perturbation of the flow, then Styrofoam plates were added around the test plate in order to be free from edge effects. The imposed heat flux ($\dot{q}$) was 581 m^2. The electric current was measured by reading from a Xantrex XPD power supply with a measurement accuracy of 11.7 mA. The voltage between two electric rods was measured using a TTI 1604 multimeter having an accuracy of 10 μV. The surface of the foil was coated with a mat black lacquer.

Table 1
Physical properties of materials

	A (mm^2)	e (μm)	α (m^2/s)	k (W/mK)
Paint		41	2.5×10^{-6}	1.0
Foil	307×461	45	4.0×10^{-6}	16.3
Epoxy		50		$\leqslant$1.0
Polyurethane	307×305, 690×480	48,000		0.07

The thermal properties of the black paint and the epoxy are estimations from the work of Praisner et al., 2001.

The measured emissivity of the paint layer was 0.94 for the spectral band of the infrared camera used (3.6–5.1 μm).

2.1. Measurements

2.1.1. Temperature measurement

The wall temperature of the upper surface of the foil was measured using infrared thermography system. This system

consisted of an infrared camera, Jade MW, a data acquisition system, CEDIP infrared systems, and infrared image processing software, Sapphire. The detector, composed of 320×240 pixels made from InSb, gives a spectral response in the middle infrared band 3.6–5.1 μm. The IR camera had a temperature resolution of 23 mK at 25 °C in terms of N.E.T.D, a dynamic resolution of 14 bits, a spatial resolution of 0.6 mrad in terms of IFOV for a 50 mm focal length lens. The IR camera was placed at a distance of 1.1 m above the test plate with an incident angle of 70° or 0°. The inclination angle did not caused hysteresis, noise and environmental influences (opposite side was painted in black to avoid environmental noise) but parallaxe of thermographic image. This deformation was corrected before calculation of heat transfer coefficient. As a consequence, the spatial resolution determined by utilized lens varied 0.6 ± 0.015 mm/pixel with an uncertainty of about 0.3%. However, this little difference is not supposed to influence on spatial resolution, generally represented as line spread function obtained by slit test. We verified also that there was no influence of inclination angle on the accuracy of measured temperature. The procedure of non-uniformity correction, bad pixel replacement of detectors and focusing of the camera were performed before measurement. The infrared camera was calibrated soon after the measurement by using an extended type differential blackbody DCN100 from HGH Infrared Systems. The blackbody's temperature was varied from 10 °C to 60 °C with an increment of 5 °C. Their thermographic images were recorded under the same environmental condition that the wall temperature measurements. This black body had an emissivity of 0.98, a temperature stability of ±0.01 K, a resolution of 0.01 K and an intrinsic error of ±0.02% + 0.02 K. The calibration random error (standard deviation equivalent to the noise level) was less than 0.04%. Conversion error of the calibration curve was negligible. During measurement and calibration, in order to minimize thermal drift, the temperature of the infrared camera was maintained constant within ±0.1 K. The standard deviation equivalent to the noise level of the infrared thermography system was ±0.014 K at the ambient temperature. The temperature of the jet (T_j) and the ambient temperature (T_{amb}) were measured with thermocouples (K-type) at the centre of the pipe exit and outside the foil (5D from the limit of the foil and 5D upwards from the exit of the pipe), respectively. These two temperature was maintained at the same and constant value.

Concerning the reproducibility of infrared thermography measurements, we obtained a standard deviation of Nusselt number of 0.64 at the stagnation point through three times measurements. In addition that, convection heat flux measured using cold wire thermometry was very approached to that of infrared thermography.

2.1.2. Energy balance at the impingement surface

Biot numbers (Bi) calculated for a range of heat transfer coefficient $30\ \mathrm{W/m^2K} < h_{cv} < 240\ \mathrm{W/m^2K}$ showed that heat conduction across the layers of paint, stainless steel foil and epoxy was negligible compared to convection ($Bi < 10^{-2}$). This was also verified by a numerical simulation using finite volume method ADI 3D solving heat equation in these layers, which gave a relative temperature difference of 0.0067% compared to the impingement surface temperature. The folded part, two ends of the foil, was neglected in the simulation because the length of this part was small (25 mm), and the measurement area was limited at 1.5D before the edge.

Using the coordinate system shown in Fig. 2, the energy balance equation for an element of stainless steel foil in steady state is given as follows:

For a volume $e_c \Delta x \Delta z$ of the top surface of the square cylinder,

$$0 = \dot{q}\Delta x\Delta z + \nabla \cdot (k_c \nabla T_p(x,0,z))\,\mathrm{d}V \tag{1}$$

where $\dot{q} = EI/A = I^2R/A$ $(\mathrm{W/m^2})$, T_p is the wall temperature.

Along y:

$$\begin{aligned} k_c \nabla T_p \cdot \vec{n}\,\mathrm{d}S = & -h_{cv}(T_p(x,0,z) - T_{ref})\Delta x\Delta z \\ & -\varepsilon\sigma[T_p(x,0,z)^4 - T_{amb}(x,0,z)^4]\Delta x\Delta z \\ & -\frac{1}{\frac{e_{is}}{k_{is}} + \frac{e_{pl}}{k_{pl}} + \frac{1}{h_{cn}}}(T_p(x,0,z) - T_{amb})\Delta x\Delta z \end{aligned} \tag{2}$$

Along x and z:

$$\nabla \cdot (k_c \nabla T_p)\,\mathrm{d}V = \frac{\partial}{\partial x}\left(k_c \frac{\partial T_p}{\partial x}\right)e_c \Delta x\Delta z + \frac{\partial}{\partial z}\left(k_c \frac{\partial T_p}{\partial z}\right)e_c \Delta x\Delta z \tag{3}$$

The subscripts c, is and pl refer to the stainless steel foil, the polyurethane insulation block and acrylic plate, respectively.

Since T_j was measured with a thermocouple at the centre of the jet exit, it corresponds to the recovery temperature (T_r) expressed as $T_r = T_s + r_c(V_{c0}^2/2c_p)$. r_c is the recovery coefficient and depends on employed thermocouple and flow. In the present study, if $r_c = 0.68$ is taken from the result of Baughn et al. (1991), the static temperature of the jet (T_s) is lower than T_{amb} by $r_c(V_{c0}^2/2c_p)$. Therefore, heat transfer coefficient is affected by entrainment flow of different temperature. In order to be free from this influence, we adopted the adiabatic wall temperature (T_{aw}) as a reference temperature (T_{ref}) in Eq. (2). This effect has been documented by a number of authors (Hollworth and Gero, 1985; Hechanova, 1986; Goldstein et al., 1990). T_{aw} was measured when the jet impinged on a non-heated test plate, then was corrected taking into account the heat losses ($q_{cd} + q_{ray} + q_{cv} = 0$) as follows:

$$\begin{aligned} T_{aw} = T_m + \frac{\varepsilon\sigma}{h_{cv}}\left(T_m^4 - T_{amb}^4\right) - \frac{k_c e_c}{h_{cv}}\left(\frac{\partial^2 T_m}{\partial x^2} + \frac{\partial^2 T_m}{\partial z^2}\right) \\ + \frac{(T_m - T_{amb})}{h_{cv}\left(\frac{e_{is}}{k_{is}} + \frac{e_{pl}}{k_{pl}} + \frac{1}{h_{cn}}\right)} \end{aligned} \tag{4}$$

where T_m is the measured infrared thermography temperature. The influence of this correction on T_{aw} was negligible (<0.0035%). The variation in T_{aw} was less than 0.1 K for the top surface and 0.2 K for the vertical and the bottom wall. To measure T_p, the test plate was gently heated by Joule heating for about one hour with jet impingement, then measurement was made in 30 minutes. During this procedure, T_{amb} had a tendency to increase by about 0.1–0.4 K. The noise of measured temperature cartography was filtered in order to calculate conduction losses. The local Nusselt number was defined as $Nu = h_{cv}D/k_{air}$. The thermal conductivity of air (k_{air}) was evaluated at film temperature $(T_p + T_{amb})/2$.

For a volume $e_c\Delta x\Delta z$ of the bottom plain plate, energy balance equation is written in the following form:

$$\begin{aligned}0 = {} & \dot{q}\Delta x\Delta z + k_c e_c\left(\frac{\partial^2 T_{p2}}{\partial x^2} + \frac{\partial^2 T_{p2}}{\partial z^2}\right)\Delta x\Delta z \\ & - h_{cv2}(T_{p2} - T_{aw2})\Delta x\Delta z \\ & - \left(\varepsilon\sigma T_{p2}^4\sum_i^{n_2}(F_{2-1})_i - \varepsilon\sum_i^{n_1}(F_{2-1}\varepsilon\sigma T_{p1}^4)_i\right)\Delta x\Delta z \\ & - \left(1 - \sum_i^{n_2}(F_{2-1})_i\right)\varepsilon\sigma(T_{p2}^4 - T_{amb}^4)\Delta x\Delta z \\ & - \left((1-\varepsilon)\varepsilon\sum_i^{n_2}(F_{2-1}\varepsilon\sigma T_{p1}^4)_i\right)\Delta x\Delta z \\ & - \frac{1}{\frac{e_{is}}{k_{is}} + \frac{e_{pl}}{k_{pl}} + \frac{1}{h_{cn}}}(T_{p2} - T_{amb})\Delta x\Delta z \end{aligned} \quad (5)$$

where the subscripts 1 and 2 refer to the vertical surface of the square cylinder and the bottom plain plate, respectively. n is the number of elements, F_{2-1} is the view factor representing a fraction of radiation leaving surface 2 intercepted by surface 1 ($dF_{2-1} = xy\,dA_1/(\pi(x^2+y^2+z^2)^2)$). Eq. (5) can be rewritten as following:

$$0 = Q_p - Q_{cv2} - Q_{r2-1} + Q_{r1-2} - Q_{r2-amb} - Q_{r1\to2\to cam} - Q_{cd2} \quad (6)$$

where

$$Q_p = \dot{q} \quad (7)$$

$$Q_{r1} = \varepsilon\sigma T_{p1}^4 \quad (8)$$

$$Q_{r2} = \varepsilon\sigma T_{p2}^4 \quad (9)$$

$$Q_{r2-1} = Q_{r2\to1} - Q_{r1\to2} \quad (10)$$

$$Q_{r1\to2} = \varepsilon\sum_i^{n1}(dA_1F_{1-2}Q_{r1})_i/dA_2 = \varepsilon\sum_i^{n1}(F_{2-1}Q_{r1})_i \quad (11)$$

$$Q_{r2\to1} = Q_{r2}\sum_i^{n2}(F_{2-1})_i \quad (12)$$

$$Q_{r2-amb} = \left(1 - \sum_i^{n2}(F_{2-1})_i\right)\varepsilon\sigma(T_{p2}^4 - T_{amb}^4) \quad (13)$$

$$Q_{r1\to2\to cam} = (1-\varepsilon)Q_{r1\to2} \quad (14)$$

$$Q_{cv2} = h_{cv2}(T_{p2} - T_{aw}) \quad (15)$$

$$Q_{cd2} = -\lambda e_c\left(\frac{\partial^2 T_p(x,0,z)}{\partial x^2} + \frac{\partial^2 T_p(x,0,z)}{\partial z^2}\right) \quad (16)$$

Energy balance equation for the vertical surface of the square cylinder is obtained in the same way that Eq. (5) with using the law of reciprocity for the view factor of radiation.

From Eqs. (1)–(3), Nusselt number uncertainty is written as the following relation:

$$\frac{\Delta Nu}{Nu} = \frac{\Delta E}{E} + \frac{\Delta I}{I} + \frac{\Delta A}{A} + \frac{\Delta T}{(T_p - T_{aw})} + \frac{\Delta D}{D} + \frac{\Delta k}{k} \quad (17)$$

which gave the maximum value 5.5% at the stagnation point.

2.2. Velocity measurement and flow visualization

Instantaneous two-dimensional velocity fields in the streamwise-wall-normal plane were measured by using PIV. A pulsed light sheet was generated with a Quantel dual Nd:YAG laser having a power of 200 mJ by pulse and a thickness of the light sheet of approximately 1 mm. Seeding of tracer particles in the flow was carried out in two ways in order to obtain a homogeneous distribution; the smoke of Armenian paper was supplied preliminarily outside then through the pipe with the jet flow. PivTec GMBH seeding device delivered DEHS particles (2-ethylhexyl-sebacat) of which the typical size is of 1μm. The image of particles, which contains superimposed PIV doublet, was registered with a 12 bits sensicam pco CCD camera at a frequency of 5 Hz. The particle image diameter was almost superior to 2 pixels for which it is generally accepted that bias error due to pick locking is the minimum. The peak-locking bias phenomenon was not found in the present study. The interval time between two consecutive images was determined between 8 μs and 80 μs according to the flow velocity, the flow structure and interrogation window size. The displacement of particles was calculated using software PIVIS developed at IMFT. The algorithm is based on cross-correlation of images using FFT method and on an iterative procedure of both the refinement of the interrogation window size and window shift. These allow a bias error of 0.1 pixel and a RMS error less than 0.16 pixels for a gradient less than 0.1 pixel/pixel. The dimension of interrogation window applied was 32×32 pixels overlapped for 50%, corresponding to approximately 1×1 mm^2 space resolution. One thousand pairs of PIV images were tested to calculate turbulence statistics, and finally 500 images were used for each measurement field. Spurious vectors were detected and eliminated if: (i) the signal-to-noise ratio is lower than 1.5, (ii) the displacement of the particles is lower than 0.1 pixel or too large compared to the neighborhood, (iii) $|(a_i - \overline{a})/\sigma_a| > 5$, where a is the measured value, σ_a is the standard deviation of a.

The reproducibility was verified through both preliminary measurements using another measurement devices and the repetition of measurements. The velocity and turbulence intensity profiles were measured for impingement region and pipe exit region several times using hot wire anemometry and verified their good superposition. The

accuracy of these results was inferior to a bias error of ±2.25% and a r.m.s error of 0.15%. Velocity at the pipe exit center was verified every time before measurement using a pitot tube within the same order of uncertainty. The reproducibility of PIV measurement was assured through both comparison with the hot wire anemometer data referred above and the repetition of measurement for recirculation region.

The oil and pigment technique was utilized to describe the flow field near to the surface. This visualization was conducted at $V_{c0} = 47.8$ m/s, two times higher than the original velocity, in order to get more visible limiting streamlines. However, the flow's topology showed the same result that under the original velocity.

3. Results and discussion

3.1. Global flow field

In the plane of symmetry $x \cdot y$, mean streamlines are shown in Fig. 3. After impingement, the flow develops on the square cylinder, then is separated. The flow reattaches downstream forming a recirculation behind the square cylinder. On the bottom plain plate, the locations of reattachment (P_R) and detachment (P_D), defined by $\overline{U}$ equal to 0, are $x/D = 6.8 \pm 0.39$ and $x/D = 3 \pm 0.61$, respectively. The amplitude of the oscillation of P_d is greater 40% than that of P_R. The oscillation of these positions has been observed by several studies in the case of BFS. A DNS study conducted by Le et al. (1997) reported that apparent large-scale roll-up of the shear layer, which is composed of many small and high-intensity counter rotating vortices, caused periodic oscillation of the reattachment position. As the large-scale structure grows, the reattachment location travels downstream. The reattachment length then suddenly decreases indicating a detachment of the turbulent large-scale structure. At that moment, the minima of pressure indicating the passage of the vortex centres was detected.

In our case, the instantaneous streamlines and vorticity field, which are not presented here, showed that the separated flow from the square cylinder repeated contraction and expansion with a non-regular sinusoidal oscillation of the centerline (Kim, 2005). Also, large-scale vortex structures were present in the shear layer. In the recirculation region close to the reattachment point, the sinusoidal oscillation of the separated flow continued. Also, three-dimensional flow showing nodes and saddle points, and vortex structures having various scales from small to large appeared. These unstable structures were distributed very randomly. Near the corner, for only $y/D < 1$, this unstable phenomenon, excepted the sinusoidal oscillation of the separated flow, were more considerably pronounced and foci were appeared. The oscillation of P_R and P_D is supposed to be caused by these unstable three-dimensional structures and the vertical oscillation of the separated flow.

According to Armaly et al. (1983), in the case of the BFS flow, the reattachment length (X_r) increases with the expansion ratio of the section (E_r). Also, X_r shows a dependency on Reynolds number Re_{H_o} based on the inlet velocity and the height of the step. X_r increases for $Re_{H_o} \leqslant 1200$ and decreases in the range $1200 < Re_{H_o} < 6600$ and then remains relatively constant for $Re_{H_o} > 6600$. In Table 2, X_r obtained by Jovic and Driver (1995) for the case of BFS flow are presented. This experiment was carried out in a wind tunnel with a two-dimensional inlet velocity profile. Our result $X_r \simeq 1.77$ has the same order of magnitude but is lower than that of BFS flow. For another experiment conducted at higher Reynolds number ($V_{c0} = 47.8$ m/s), we obtained the same X_r like the trend of BFS flow. Since the separated jet from the square cylinder is spread axisymmetrically, spanwise momentum exchange could be important. On the other hand, that will cause a decrease of streamwise kinetic energy and result in a decrease of X_r.

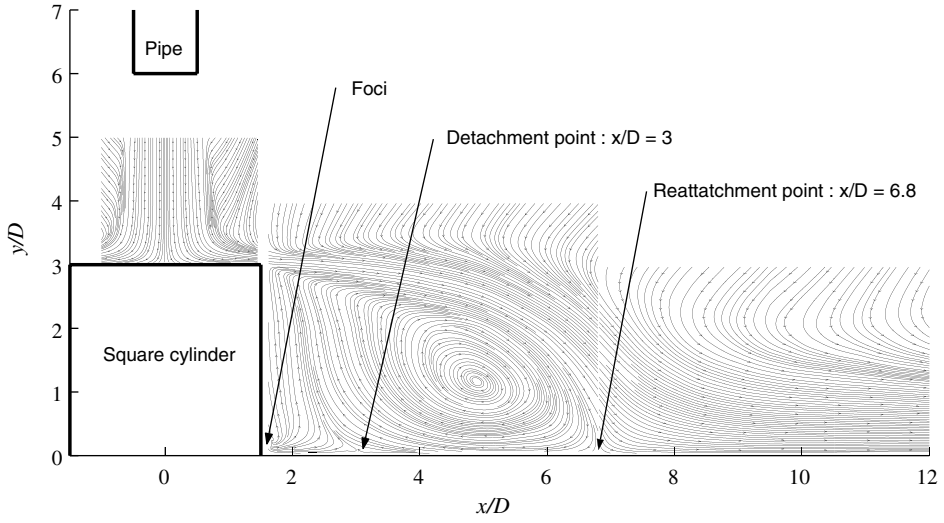

Fig. 3. Mean streamlines at the plane $x \cdot y$ at $z = 0$.

Table 2
Length of reattachment X_r for BFS flow from Jovic and Driver (1995)

Re_{H_o}	δ/H_o	Re_θ	U_0 (m/s)	h (mm)	E_r	X_r/H_o
5000	1.20	600	7.70	9.65	1.20	6.00
6800	2.00	1650	6.00	17.0	1.09	5.35
10,400	1.27	1650	6.00	26.0	1.14	6.35
25,500	1.20	3600	14.60	26.0	1.14	6.90
25,500	0.82	2400	10.00	38.0	1.20	6.84
37,200	0.82	3600	14.60	38.0	1.20	6.84
37,500	1.50	5000	44.20	12.7	1.11	6.26

U_0 inlet velocity, H_o height of the step, δ boundary layer thickness in inlet, $Re_{H_o} = U_0 H_o/\nu$, E_r expansion ratio of the section.

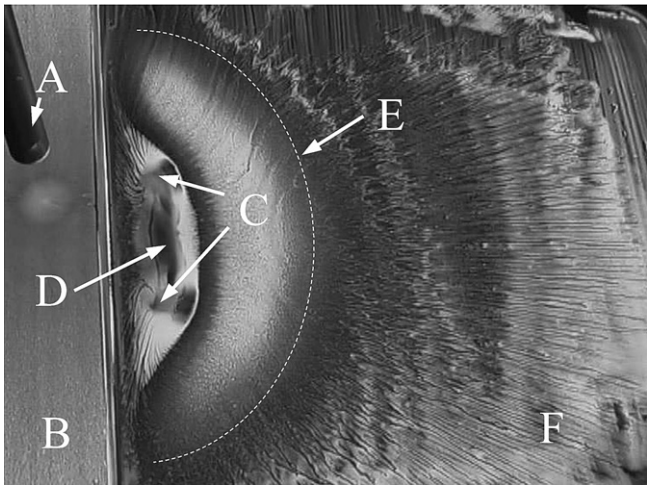

Fig. 4. Flow visualization on the wall. A: pipe, B: cylinder, C: foci, D: detachment line, E: reattachment line, F: flat plate.

Near the vertical wall of the square cylinder, mean streamlines show that a flow comes out of a repelling focus at the corner ($x/D = 1.68$, $y/D = 0.23$) then moves upward. This flow's topology differ significantly from the secondary vortex typically found in traditional BFS flow. This flow was more examined with the oil-pigment flow visualization result for the bottom plain plate. In Fig. 4, the presence of a flow traversing $x \cdot y$ plane and moving toward the corner of the plane of symmetry is clearly showed. Since the recirculation flow is symmetric to the $x \cdot y$ plane and have a quasi-axisymmetric shape, they are oriented to the corner of the plane of symmetry, then their first collision makes the flow to go toward x and y direction. The second collision between this flow and the recirculation toward the square cylinder results in symmetric two attracting foci and detachment line. The schematic of the flow obtained by flow visualizations using styrofoam particles at $Re_j = 23{,}000$ is shown in Fig. 5. The distance between the centre of the symmetric foci was $4D$.

3.2. Heat transfer and turbulence statistics

Fig. 6 shows Nusselt number distributions for the top wall of the square cylinder. The maximum of Nu is found

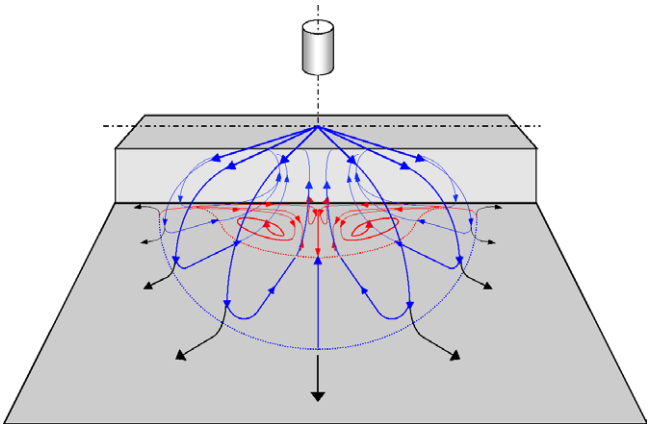

Fig. 5. Schematic diagram of the flow structure.

at the stagnation point. The increase of Nu was observed on the edge, and that is due to the negative conduction heat loss on the surface. However, high gradient of temperature and the limit of camera spatial resolution made increased uncertainty of measurement in this region since the evaluation of heat conduction was very sensitive at noise.

Three results obtained when heat was lost only by convection (Q_{cv}) or by convection and radiation (Q_r) or convection, radiation and conduction (Q_c) are considered in the energy balance equation, are plotted in Fig. 6(b) and (c). In Fig. 6(c), a secondary peak appears at $z/D = 2.21$. This local maximum has been observed by a number of previous works in the case of the jet impinging on a flat plate when jet-to-plate spacing is relatively small ($H/D < 6$), and its origin has been one of the most commented subject (Baughn and Shimizu, 1989; Kim, 2005). To analyze the effect of H, in Fig. 7, the evolutions of v'/V_j, w'/V_j, $\overline{vw}/V_j^2$ and $\bar{k}/V_j^2$ ($\bar{k} = (v'^2 + w'^2)/2$) measured at a distance of $0.1D$ from the wall are compared with those for $H/D = 6$, of which the experiment was conducted for a plain impingement plate by Kim (2005). In the first half of the impingement region ($0 < z/D < 1$), the levels of these quantities for $H/D = 3$ are lower and the distribution is less homogeneous than for $H/D = 6$. Due to the short spacing H, turbulence was less diffused. In contrast, in the second half of the impingement region ($1 < z/D < 2$), the increase rate of these values is very remarkable. The maxima are not only higher (27.08 % in w', 47.33% in v' and 20.43% in $\overline{vw}$) but also more localized at $z/D = 2$. While, v'/V_j and $\overline{vw}/V_j^2$ for $H/D = 6$ exhibited local minima at this position, their maxima are found downstream ($z/D \simeq 2.5$). Mixing with surrounding air was thus particularly important at $z/D = 2$ for $H/D = 3$. Beyond $z/D = 3$, there was little difference between the two results (Giovannini and Kim, 2006).

In Fig. 8, the distributions of the production of turbulent kinetic energy P_k for $H/D = 3$ and 6 are shown $\left(P_k = -\left[\overline{vw}\left(\frac{\partial \overline{V}}{\partial z} + \frac{\partial \overline{W}}{\partial y}\right) + \overline{w^2}\frac{\partial \overline{W}}{\partial z} + \overline{v^2}\frac{\partial \overline{V}}{\partial y}\right]\right)$. In the two figures, near the stagnation point, we find commonly negative production principally due to $-\overline{w^2}\frac{\partial \overline{W}}{\partial z}$. The impingement,

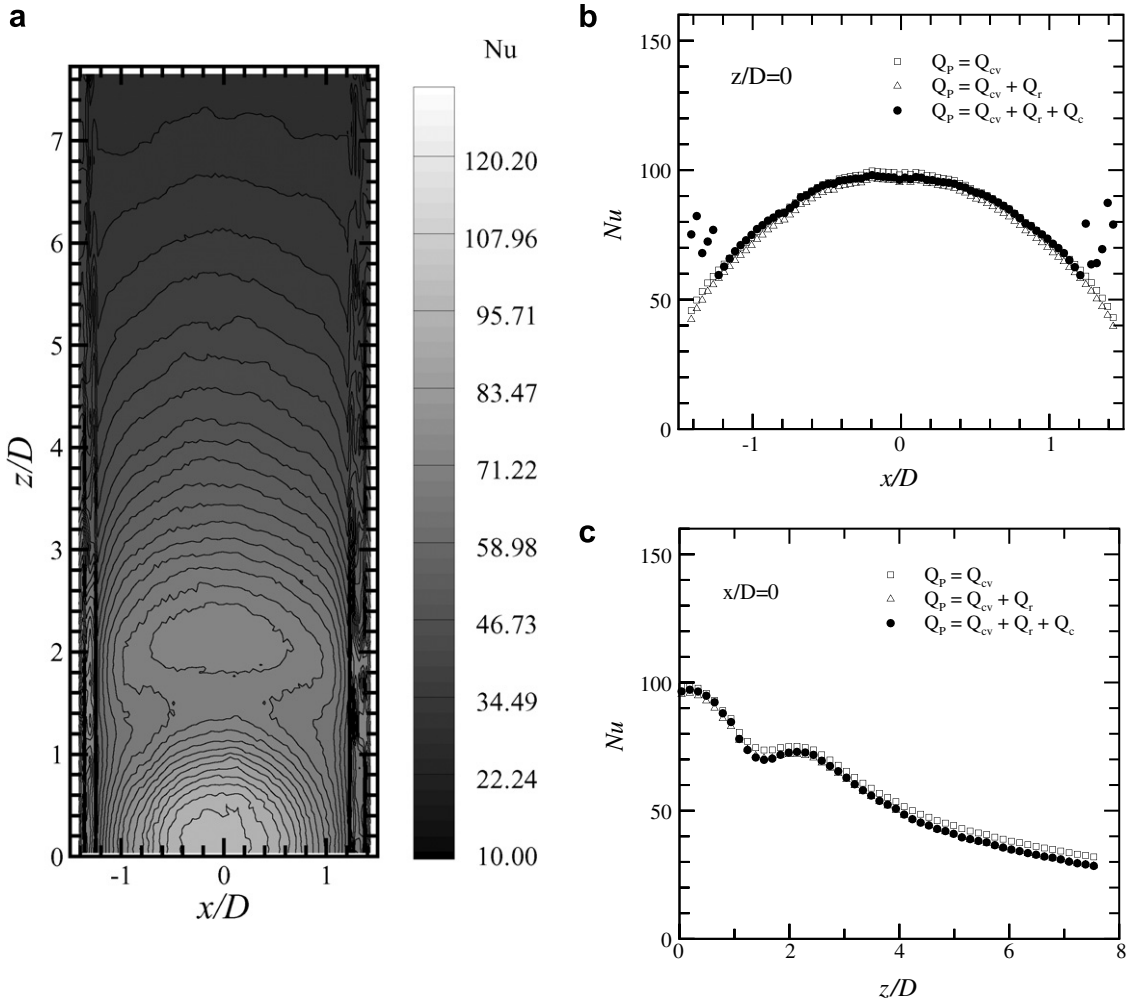

Fig. 6. Nusselt number distribution for the top wall of the square cylinder (a) on the surface, (b) along x, (c) along z.

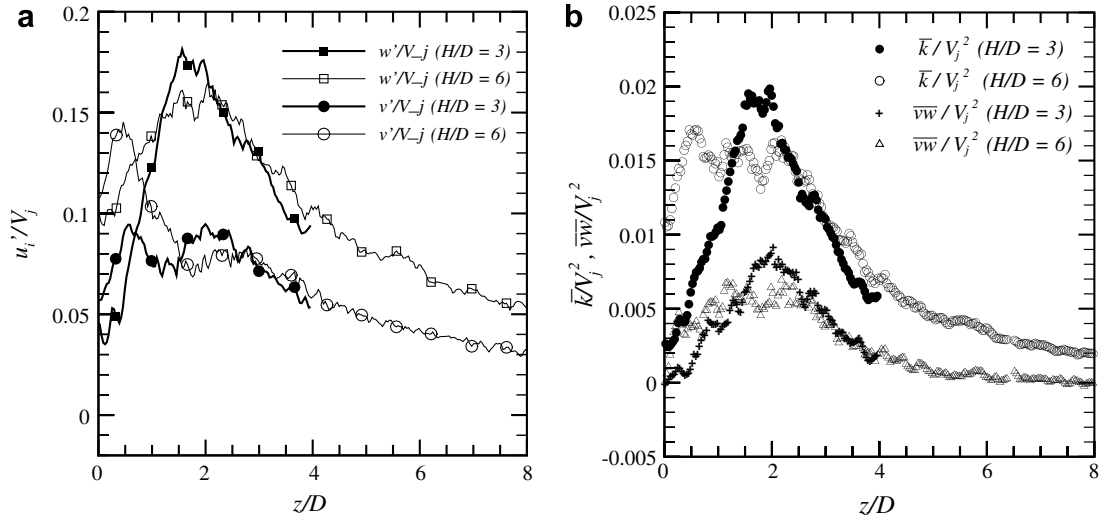

Fig. 7. Comparison of the evolutions for $H/D = 3$ and 6 along z at a distance of $0.1D$ from the wall. (a) w'/V_j and v'/V_j, (b) $\overline{vw}/V_j^2$ and $\bar{k}/V_j^2$. (○, △, □, Kim (2005)).

stagnation and redirection convert turbulent kinetic energy into mean kinetic energy. According to Nishino et al. (1996), the increase of w' and W, and the decay of v' and V, which is remarked in Fig. 7, are related to the net momentum transport from the turbulent velocity field to the static pressure. Compared to that for $H/D = 6$, the

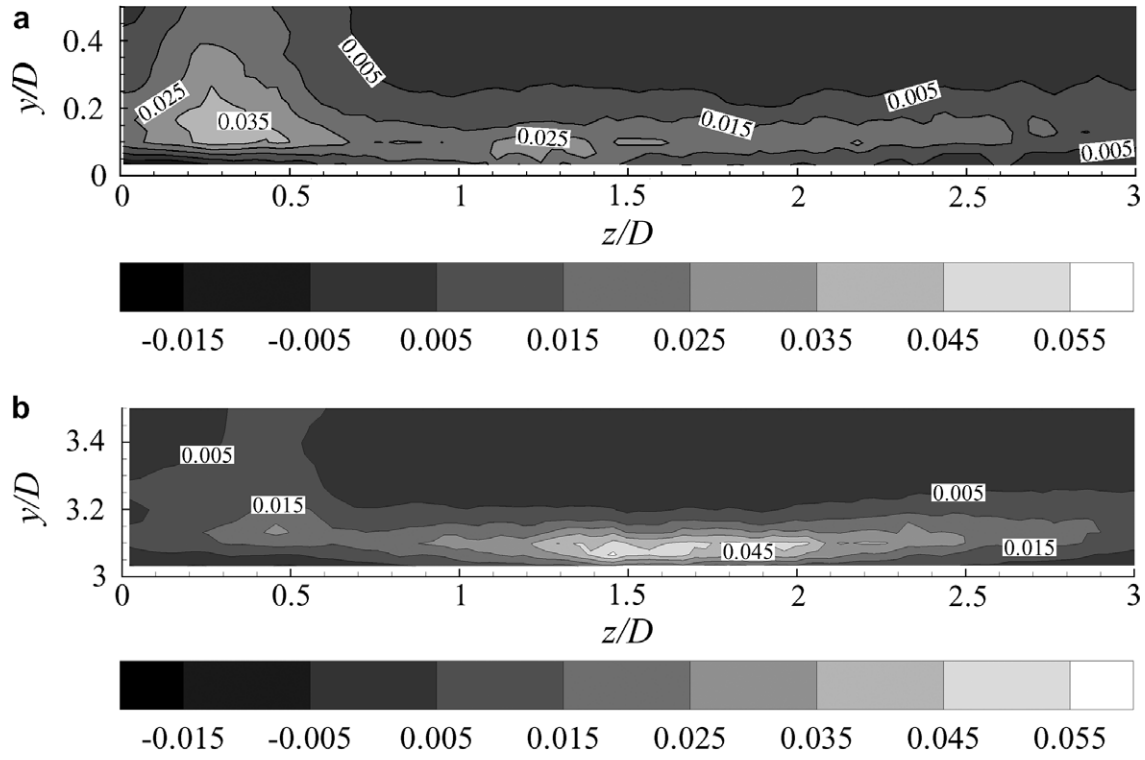

Fig. 8. Distribution of the production term of turbulent kinetic energy adimensioned $P_k \frac{D}{V_j^3}$: (a) $H/D = 6$ for the flat impingement plate from Kim (2005) and (b) $H/D = 3$ along z.

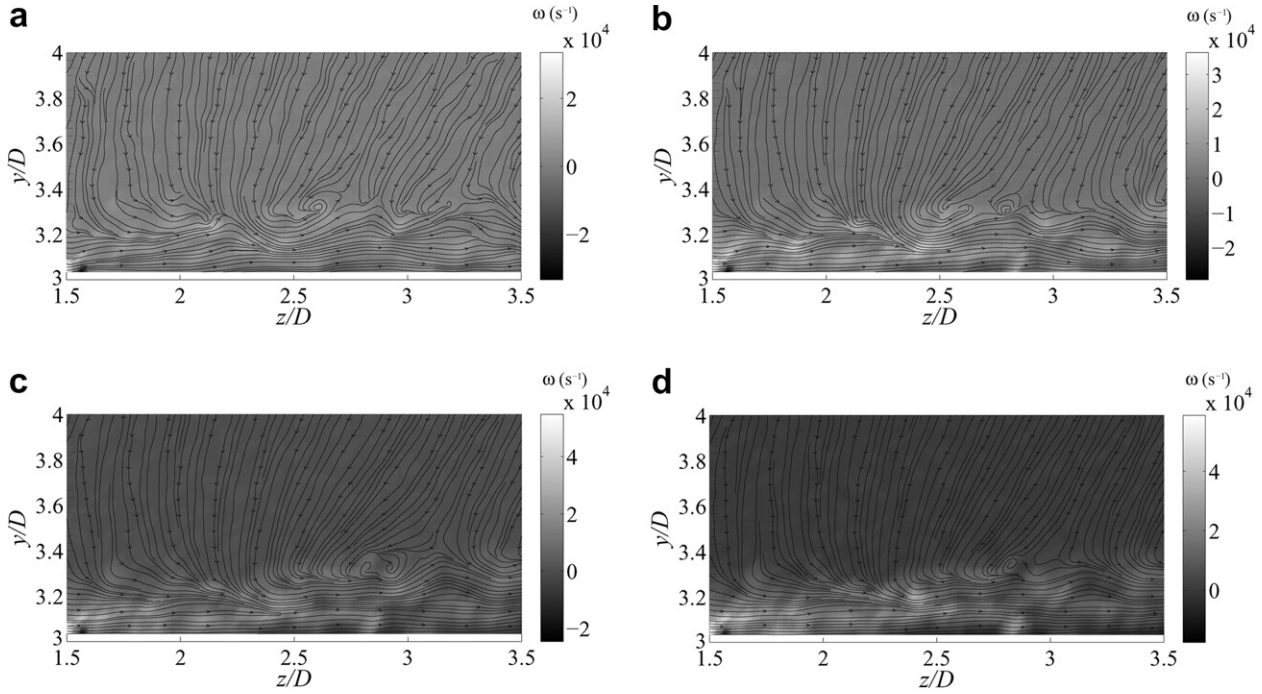

Fig. 9. Instantaneous vorticity field and stream lines at the plane $y \cdot z$ and $x = 0$ (inter-figure frequency: 5 Hz).

important differences for $H/D = 3$ are: (i) Relatively small P_k around $z/D = 0.3$ due to a lower value of $-\overline{v^2}\frac{\partial \overline{V}}{\partial y}$ eventually lower v'. On the other hand, the maximum of P_k for $H/D = 6$ was attained in the shear layer of the impinging jet. (ii) Outstanding increase of P_k in the region $1.5 < z/D < 2$ principally due to high level shear production $-\overline{vw}(\partial \overline{W}/\partial y)$. The maximum of production is about 2 times higher than for $H/D = 6$. Since the relatively short jet-to-

plate spacing do not give enough time for developing turbulence, the production of turbulent kinetic energy occurred downward than that for $H/D = 6$. For all two cases, P_k in the wall jet region was dominated by shear production term, but for $H/D = 6$ the local maximum was located forward than for $H/D = 3$, at around $z/D = 1.2$.

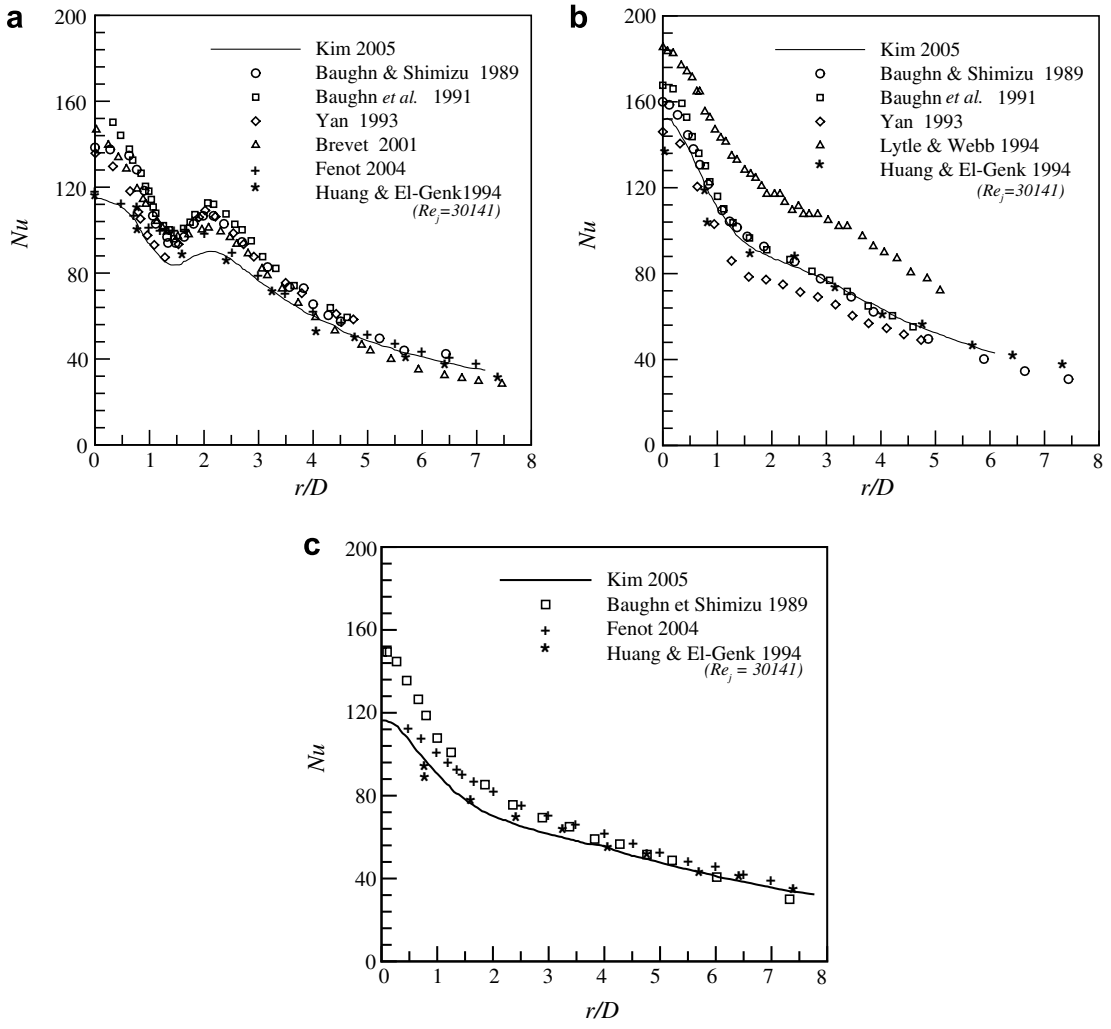

Fig. 10. Nusselt number distribution for the case of jet impinging on a flat plate. (a) $H/D = 2$, (b) $H/D = 6$, (c) $H/D = 10$ (Kim, 2005; Baughn and Shimizu, 1989; Baughn et al., 1991; Brevet, 2001; Fenot, 2004; Huang and El-Genk, 1994; Lytle and Webb, 1994).

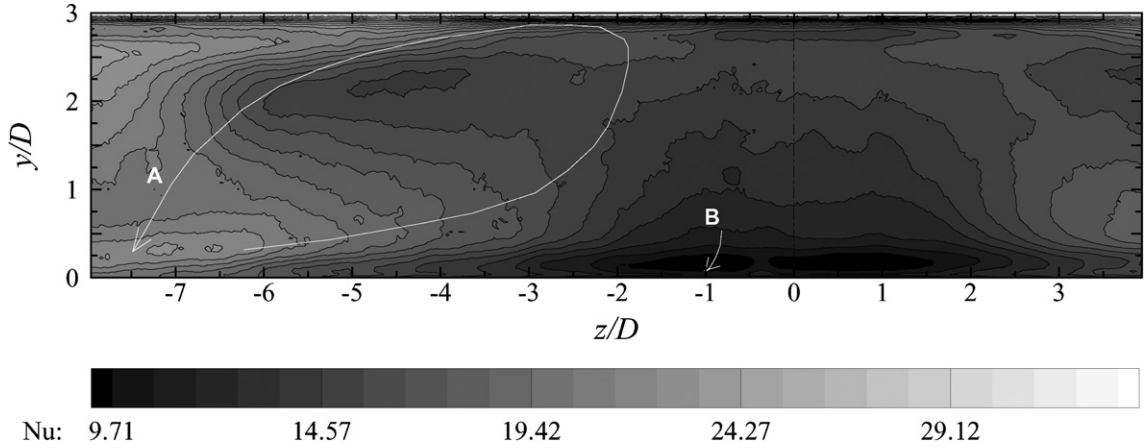

Fig. 11. Nusselt number distribution for the vertical wall of the square cylinder.

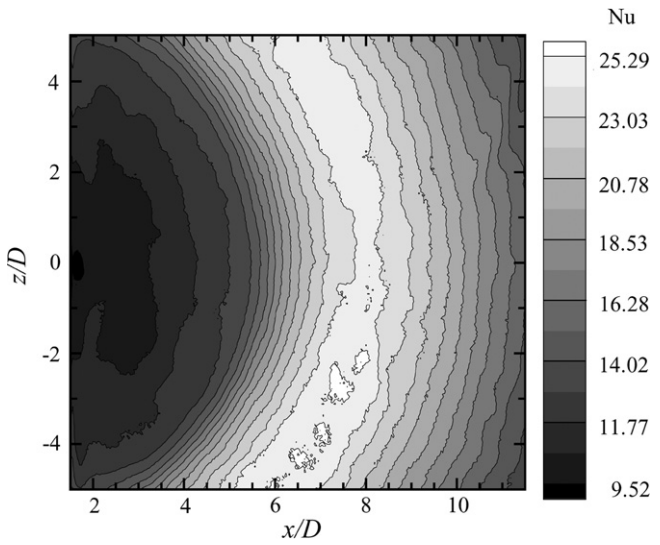

Fig. 12. Nusselt number distribution for the bottom wall.

Instantaneous streamlines (Fig. 9) show that the flow structures are similar to the structures related to both the ejection and the sweep processes in the boundary layer.

In Fig. 10, published results about Nusselt number distributions for the case of jet impinging on a flat plate (Kim, 2005; Baughn and Shimizu, 1989; Baughn et al., 1991; Brevet, 2001; Fenot, 2004; Huang and El-Genk, 1994; Lytle and Webb, 1994) are compared for different jet-to-plate spacing H. Despite similar heat transfer behaviour among experimental data, the dispersion in the magnitudes of Nu is significant and problematic. Different experimental conditions and definition of heat transfer coefficient are supposed to be the reason of this discrepancy. More detailed explanation about this is presented in Kim (2005) and Giovannini and Kim (2006). Compared to the results of Kim (2005), Nusselt number at the stagnation point for the case of square cylinder (Fig. 6) is in the same order of value but a little less than those for $H/D = 2$, 6 and 10. It is known that heat transfer coefficient at stagnation point decreases after $H/D \approx 2$ and then increase after local minimum until $H/D \approx 6$. This tendency is showed also in our result. In addition to that, recirculation flow beyond the square cylinder could influence the temperature of entrained flow into the impinging jet, which cause the decrease of heat transfer coefficient.

Figs. 11 and 12 show the distributions of Nu for the vertical wall and the bottom wall. They show a good coherence with the flow visualization presented above. For the vertical wall, heat loss by convection in the region $|z/D| \leqslant 7$ is mainly influenced by the recirculation flow parallel to the wall (the flow direction was marked A in Fig. 11). The core of this recirculation can be noticed by relatively low Nu. Although this recirculation is not completely closed, relatively entrapped heat leads to a higher local temperature. Beyond the reattachment point ($z/D = \pm 6.8$), Nu becomes higher and more homogeneous in y direction due to higher velocity of the flow. On the other hand, in the vicinity of the axis of symmetry, Nu is relatively low due to low velocity (Fig. 14). At the corner $y/D = 0.25$, Nu becomes minimum. This region coincides with the location of the foci shown in the mean streamlines of Fig. 3, below which the mean flow moves toward the

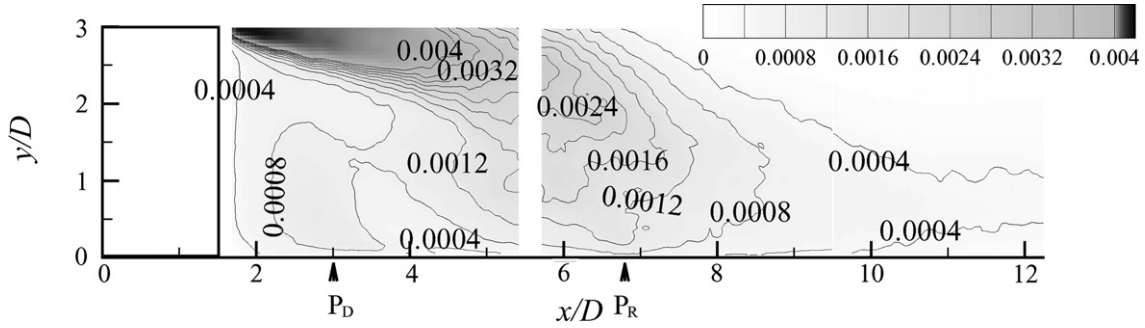

Fig. 13. Distribution of normalized mean turbulent kinetic energy $\bar{k}/V_j^2$. $k = \frac{1}{2}(u'^2 + v'^2)$.

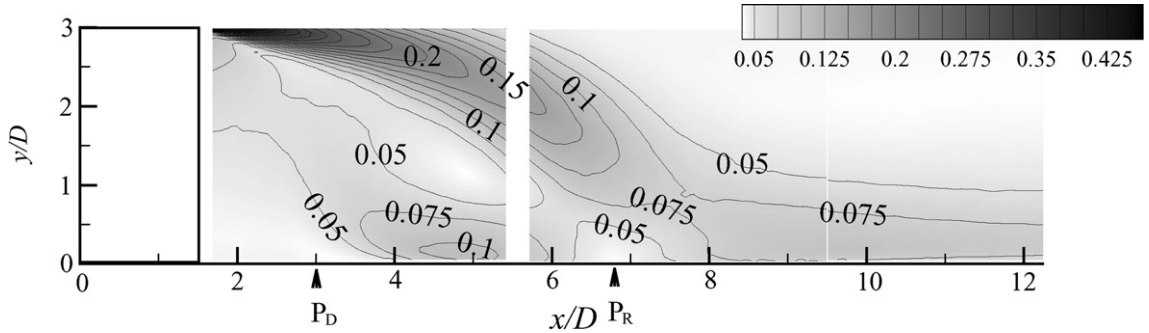

Fig. 14. Distribution of normalized mean velocity $\overline{U}_m/V_j$. $\overline{U}_m = (\overline{U}^2 + \overline{V}^2)^{0.5}$.

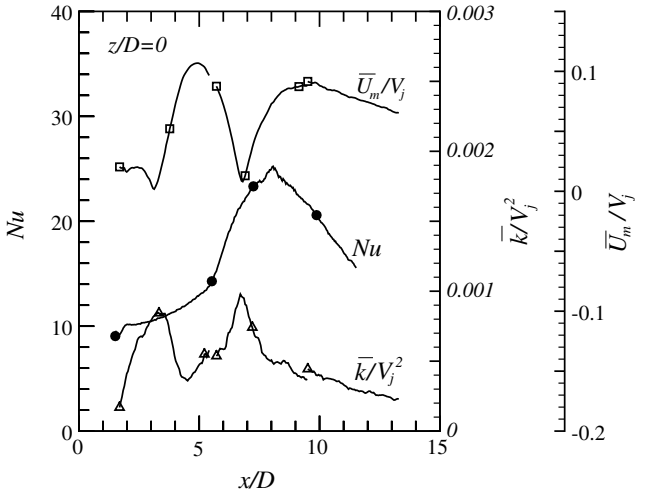

Fig. 15. Distributions of Nusselt number and $\overline{k}/V_j^2$ and $\overline{U}_m/V_j$ at $y/D = 0.1$ for the bottom wall at $z/D = 0$.

bottom wall (marked B). The coldest region is situated in the vicinity of the higher edge because of high velocity separation flow and entrainment. In this region, the temperature gradient is very high. Globally, heat losses by conduction and radiation vary between −9% and 34%, and between −1.6% and 3.3% of $\dot{q}$, respectively.

For the bottom wall, we find a semi-circular distribution of *Nu*, consistent with the shape obtained by flow visualization. Two local minima at $2 < z/D < 3$ coincide with the location of symmetrical foci (Fig. 12) that entrapped heat leads to a higher local temperature. The maximum of *Nu* (equal to 25.8) is located at the vicinity of $x/D = 8$, which is $1.2D$ downstream compared to P_R. Fig. 13 shows that the turbulent kinetic energy attains its maximum at P_R on the near-wall. The discrepancy between the two positions is due to the fact that the reattachment position corresponds to the border of the flow impinging on the bottom wall. In Fig. 14 we find that the centreline of the reattaching flow go ahead to around $x/D \simeq 8$ at $y/D = 0$ which corresponds to the maximum of *Nu*. The minimum of *Nu* (equal to 10) is found on the corner of the axis of symmetry. The heat losses by conduction and radiation corresponds respectively to the values between −2.6% and 7.7%, and −0.5% and 1.82% of $\dot{q}$.

In Fig. 15, distributions of Nusselt number and $\overline{k}/V_j^2$ and $\overline{U}_m/V_j$ at $y/D = 0.1$ for the bottom wall at $z/D = 0$ are compared. This figure shows that local heat transfer is influenced by both turbulent kinetic energy and kinetic energy. Because of the competition of these two quantities, it is difficult to make a quantitative correlation between local heat transfer coefficient and flow characteristic. Mean values of *Nu* for three faces are given in Table 3.

Table 3
Mean Nusselt number in the three regions for $0 \leqslant z/D \leqslant L_z$

	Zone 1		Zone 2		Zone 3	
L_z/D	5	7	5	7	5	7
Nu	62.2	54.1	17.8	–	15.4	16.5

Zone 1: $0 \leqslant x/D \leqslant 1.4$, zone 2: $x/D = 1.5$ and $0 \leqslant y/D \leqslant 2.99$, zone 3: $1.5 \leqslant x/D \leqslant 11.5$.

4. Conclusion

PIV measurement, flow visualization close to the wall and temperature measurement using infrared thermography provided a global understanding of the flow and the heat transfer rate. Jet flow impinging on a heated square cylinder mounted on a flat plate showed a three-dimensional recirculation flow, which is significantly different in topology compared to traditional BFS flow. The mean flow showed relatively short reattachment length and symmetric foci on the bottom wall near the corner due to the interaction of recirculation flows. A good coherence between flow field and heat transfer distribution was found for the vertical and bottom wall. In the impingement region on the top wall, local maximum of heat transfer coefficient was related to an analysis of turbulence statistics and turbulent kinetic energy balance.

The present study was the first step in the comprehension of heat transfer process related to jet impinging on a square cylinder. In future work, we will investigate the influence of jet position on heat transfer for an eventual optimization of heat transfer.

References

Armaly, B.F., Durst, F., Pereira, J.C.F., Schönung, B., 1983. Experimental and theoretical investigation of backward-facing step. J. Fluid Mech. 127, 473–496.

Baughn, J.W., Hechanova, A.E., Yan, X., 1991. An experimental study of entrainment effects on the heat transfer from a flat surface to a heated circular impinging jet. ASME J. Heat Transfer 113, 1023–1025.

Baughn, J.W., Shimizu, S., 1989. Heat transfer measurements from a surface with uniform heat flux and an impinging jet. ASME J. Heat Transfer 111, 1096–1098.

Brevet, P., 2001. Etude experimentale et numérique des transferts thermiques par impact de jet(s) application aux moteurs aéronautiques. Thèse de doctorat, Université de Poitiers.

Cooper, D., Jackson, D.C., Launder, B.E., Liao, G.X., 1993. Impinging jet studies for turbulence model assessment 1. Flow-field experiments. Int. J. Heat Mass Transfer 36 (10), 2675–2684.

Cornaro, C., Fleischer, A.S., Goldstein, R.J., 1999. Flow visualization of a round jet impinging on cylindrical surfaces. Exp. Thermal Fluid Sci. 20, 68–78.

Fenot, M., 2004. Etude du refroidissement par impact de jets. application aux aubes de turbines. Thèse de doctorat, Université de Poitiers.

Gau, C., Chung, C.M., 1991. Surface curvature effect on slot-air-jet impingement cooling flow and heat transfer process. ASME J. Heat Transfer 113, 858–864.

Giovannini, A., Kim, N.S., 2006. Impinging jet: experimental analysis of flow field and heat transfer for assement of turbulence models. In: 13th International Heat Transfer Conference, Sydney, Australia, 13–18 August.

Goldstein, R.J., Sobolik, K.A., Seol, W.S., 1990. Effect of entrainment on the heat transfer to a heated circular air jet impinging on a flat surface. ASME J. Heat Transfer 112, 608–611.

Hechanova, T.E., 1986. An experimental study of entrainment effects on heat transfer from a surface with a fully developed impinging jet. Thesis b. s., University of California.

Hollworth, B.R., Gero, L.R., 1985. Entrainment effects on impingement heat transfer: Part ii – local heat transfer measurements.. ASME J. Heat Transfer 107, 910–915.

Hrycak, P., 1981. Heat transfer from a row of jets impinging on concave semi-cylindrical surfaces. Int. J. Heat Mass Transfer 28, 175–181.

Huang, L., El-Genk, M.S., 1994. Heat transfer of an impinging jet on a flat surface. Int. J. Heat Mass Transfer 37 (13), 1915–1923.

Igarashi, T., 1985. Heat transfer from a square prism to an air stream. Int. J. Heat Mass Transfer 28 (1), 175–181.

Igarashi, T., 1986. Local heat transfer from a square prism to an air stream. Int. J. Heat Mass Transfer 29 (5), 774–784.

Igarashi, T., 1987. Fluid flow and heat transfer around rectangular cylinders (the case of a width/height ratio of a section of 033:1.5). Int. J. Heat Mass Transfer 30 (5), 893–901.

Jovic, S., Driver, D.M., 1995. Reynolds number effects on the skin friction in separated flows behind a backward facing step. Exp. Fluids 18, 464–467.

Kim, N.S., 2005. Analyse expérimentale d'un jet turbulent impactant sur une plaque plane et sur un obstacle de section carrée. Thèse de doctorat, Université Paul Sabatier Toulouse III.

Le, H., Moin, P., Kim, J., 1997. Direct numerical simulation of turbulent flow over a backward-facing step. J. Fluid Mech. 330, 349–374.

Lytle, D., Webb, B.W., 1994. Air jet impingement heat transfer at low nozzle-plate spacings. Int J. Heat Mass Transfer 37 (12), 1687–1697.

Martin, H., 1977. Heat and mass transfer between impinging gas jets and solide surfaces. Adv. Heat Transfer 13, 1–60.

Martinuzzi, R., Tropea, C., 1993. The flow around surface-mounted, prismatic obstacles placed in a fully developed channel flow. J. Fluids Eng. 115, 85–92.

Mesbah, M., 1996. An experimental study of local heat transfer to an impinging jet on nonflat surfaces: a cylindrical pedestal and a hemispherically concave surface. Ph.D thesis, University of California, Davis, CA.

Molki, M., Faghri, M., Ozbay, O., 1995. A correlation for heat transfer and wake effect in the entrance region of an in-line array of rectangular blocks simulating electronic components. ASME J. Heat Transfer 117, 40–46.

Nishino, K., Samada, M., Kasuya, K., Torii, K., 1996. Turbulence statistics in the stagnation region of an axisymmetric impinging jet flow. Int. J. Heat Fluid Flow 17 (3), 193–201.

Parneix, S., Behnia, M., Durbin, P., 1999. Predictions of turbulent heat transfer in an axisymmetric jet impinging on a heated pedestal. ASME J. Heat Transfer 121, 43–49.

Praisner, T.J., Sabatino, D.R., Smith, C.R., 2001. Simultaneously combined liquid crystal surface heat transfer and PIV flow-field measurements. Exp. Fluids 30, 1–10.

Viskanta, R., 1993. Heat transfer to impinging isothermal gas and flame jets. Exp. Thermal Fluid Sci. 6, 111–134.